

BEAMLET EXPERIMENTS

P. Wegner

B. Van Wonterghem

S. Burkhart

C. Widmayer

J. Murray

The Beamlet laser is a single-aperture, nearly full-scale physics prototype of the 192-beam Nd:glass laser driver for the National Ignition Facility (NIF).¹ It employs a multipass amplifier architecture similar to the design of a single NIF beamline. As shown in Figure 1, the laser system consists of a preamplifier followed by two large amplifier stages: a four-pass cavity amplifier and a single-pass booster amplifier. The cavity amplifier contains eleven side-pumped Brewster's angle slabs situated at one end of a 36-m-long image-relayed cavity formed by a spatial filter and two end mirrors. The pulse from the preamplifier is injected near the focal

plane of the spatial filter and makes four passes through the slabs before being ejected from the cavity by a full-aperture plasma-electrode Pockels cell and polarizer. The five-slab-long booster amplifier provides additional amplification and delivers typically 12 kJ in 3 ns, the Beamlet design point. The beam is then spatially filtered and relayed to the final optics, where it is frequency-converted to the third harmonic and focused to an equivalent NIF target plane. Comprehensive diagnostics at the input and output of the main amplifier provide beam data for gauging system performance at both 1.053- μm (1ω) and 0.351 (3ω) wavelength.^{2,3}

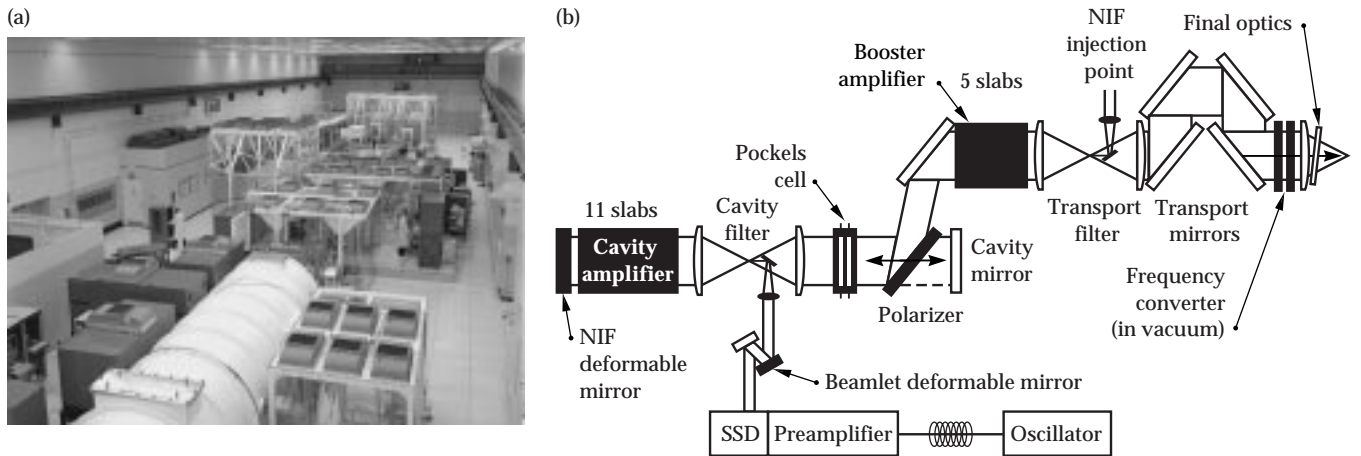


FIGURE 1. (a) Photo of the Beamlet facility taken from the output end of the laser, showing the test mule and focal-plane diagnostic (foreground) used for third-harmonic experiments. (b) Diagram of the Beamlet prototype laser showing relative locations of major components. (70-50-1297-2574pb01)

Beamlet's design diverges from the NIF's in three important and quantifiable ways:

1. A smaller clear aperture (36 vs 40 cm).
2. Injection of the Beamlet pulse into the 18-m-long cavity filter (vs injection of the NIF pulse into the 60-m-long transport filter).
3. An adaptive optics system that utilizes a 7-cm deformable mirror at the output of the preamplifier (vs the 40-cm deformable mirror that will be deployed at the cavity first-mirror position on NIF).

In addition, the Beamlet master oscillator and preamplifier are non-prototypical of NIF, although they share certain modern design features. Nonetheless, Beamlet has proven to be an essential test bed for evaluating laser physics and component engineering issues related to the NIF.

The primary mission for Beamlet has been the integrated testing of NIF laser technologies. Since its activation milestone in September 1994, Beamlet has produced over one thousand full-system shots in over twenty experimental campaigns addressing a broad range of technical issues relating to high-power beam propagation, high-energy temporally shaped pulses, spatial filtering, wavefront control, final optics, and frequency conversion. Experiments in high-power beam propagation established NIF *B*-integral limits and spatial-filter requirements for controlling nonlinear ripple growth and beam breakup. Experiments in pulse shaping produced the high-contrast, high-fluence 20-ns shaped 1 ω pulses required for the NIF ICF mission. Experiments addressing spatial-filter issues established the pressure limits for NIF spatial filters, and demonstrated new pinhole designs that are effective in mitigating closure and back reflections under NIF operating conditions. Experiments in wavefront control demonstrated ability to meet NIF focusing requirements and provided a baseline for establishing finishing specifications for NIF optical components. Final optics experiments evaluated prototype UV

components in NIF-like configurations at high fluence and demonstrated high-efficiency frequency conversion to the third harmonic using crystals fabricated with both conventional and rapid-growth technology. The following sections describe each of these activities.

High-Power Pulse Propagation

The control of nonlinear ripple growth leading to beam breakup is an essential part of the design and operation of high-power solid-state lasers.⁴ The mechanism of concern is the intensity-dependent refractive index in the laser components, which enables a weak ripple wave copropagating with a strong pump wave to couple and scatter a third wave conjugate in angle to the ripple.⁵⁻⁷ Subsequent interaction of the conjugate wave with the pump feeds back and amplifies the ripple wave leading eventually to the unstable generation of higher-order ripple modes, self-focusing, and beam breakup.

Methods of mitigating ripple growth are limited, but critical for producing high-quality beams with safe modulation levels. Optical components must comply with stringent specifications for homogeneity and surface finish to limit the source of phase perturbations, which cause small-scale amplitude modulation. Growth of these source terms depends on the *B*-integral, or intensity-dependent phase retardation allowed between spatial-filter pinholes (ΔB), and is limited by pinhole sizing.

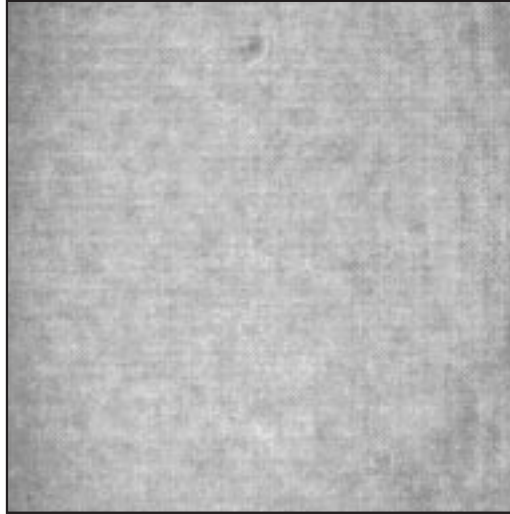
Near-field modulation experiments were conducted on Beamlet to establish the *B*-integral limits and spatial filtering requirements for the NIF. By propagating 200-ps pulses through the laser under conditions equivalent to those expected during a 20-ns ICF ignition pulse, we obtained "snap shots" of beam quality that might otherwise be masked by temporal integration effects in the diagnostics. The reduced gain and high *B*-integral that occur during the most stressful period near the end of the ignition pulse were simulated by conducting the majority of the tests with the

booster amplifiers turned off. This configuration mimics the most severe condition in which the pulse has extracted all the energy from the booster amplifiers.

A metric for evaluating beam quality is the beam contrast, defined as the standard deviation of the near-field irradiance divided by the mean. Contrast was measured for various pinhole sizes as a function of the B -integral accumulated between the Pass-4 pinhole in the cavity spatial filter and the pinhole plane of the transport spatial filter, ΔB . Initial tests were conducted without a pinhole in the transport spatial filter to evaluate beam contrast at the input lens of the spatial filter, where the risk of 1ω damage is highest. Figure 2 shows examples of the resulting near-field irradiance data obtained at low and high B -integral. The dependence of contrast on ΔB is plotted in Figure 3a for two different cavity pass-4 pinhole sizes corresponding to acceptance angles of $\pm 200 \mu\text{rad}$ and $\pm 130 \mu\text{rad}$. Open points in the plot represent shot data, and solid points are the result of numerical simulation. The onset of rapid deterioration in beam quality occurs at lower ΔB with the larger pinhole. At a ΔB of approximately 2 rad, the 200- μrad data has begun a rapid ascent towards beam breakup while the 130- μrad data is still in the slowly varying region of the curve. Thus for $\Delta B < 2$, cavity pinhole sizes of 200 μrad or smaller are acceptable, but with smaller pinholes the margin for error is substantially increased.

Figure 3b plots the contrast that results at the output relay plane of the laser when a pinhole is used in the transport spatial filter. In this case there is discrepancy between the test data and the simulations that is attributed to incomplete characterization of the noise fields in the preamplifier. Nonetheless, both show that the beam contrast should remain small for ΔB as high as 3 rad if the pinhole size in the filters is reduced from 200 to $\sim 100 \mu\text{rad}$. Reducing pinhole size is a challenge because it increases the risk of closure for long pulses (see the section Spatial Filtering on p. 47). For $\Delta B < 1.8$ rad, the contrast is < 0.08 and, within error, is independent of pinhole size below 200 μrad . This result is the origin of the 0.1-contrast specification and 1.8-rad ΔB limit for the NIF.

(a) $\Delta B = 0.9$



(b) $\Delta B = 2.6$

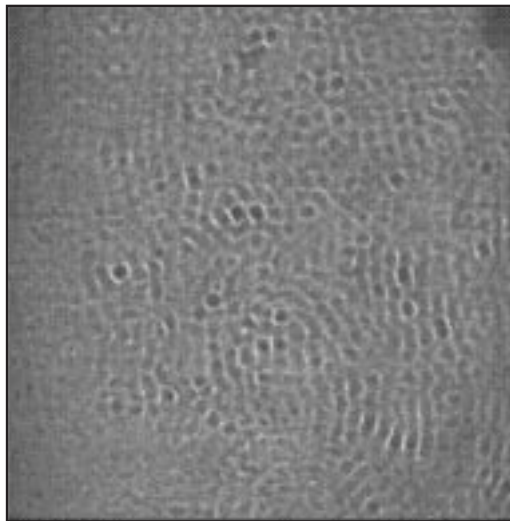
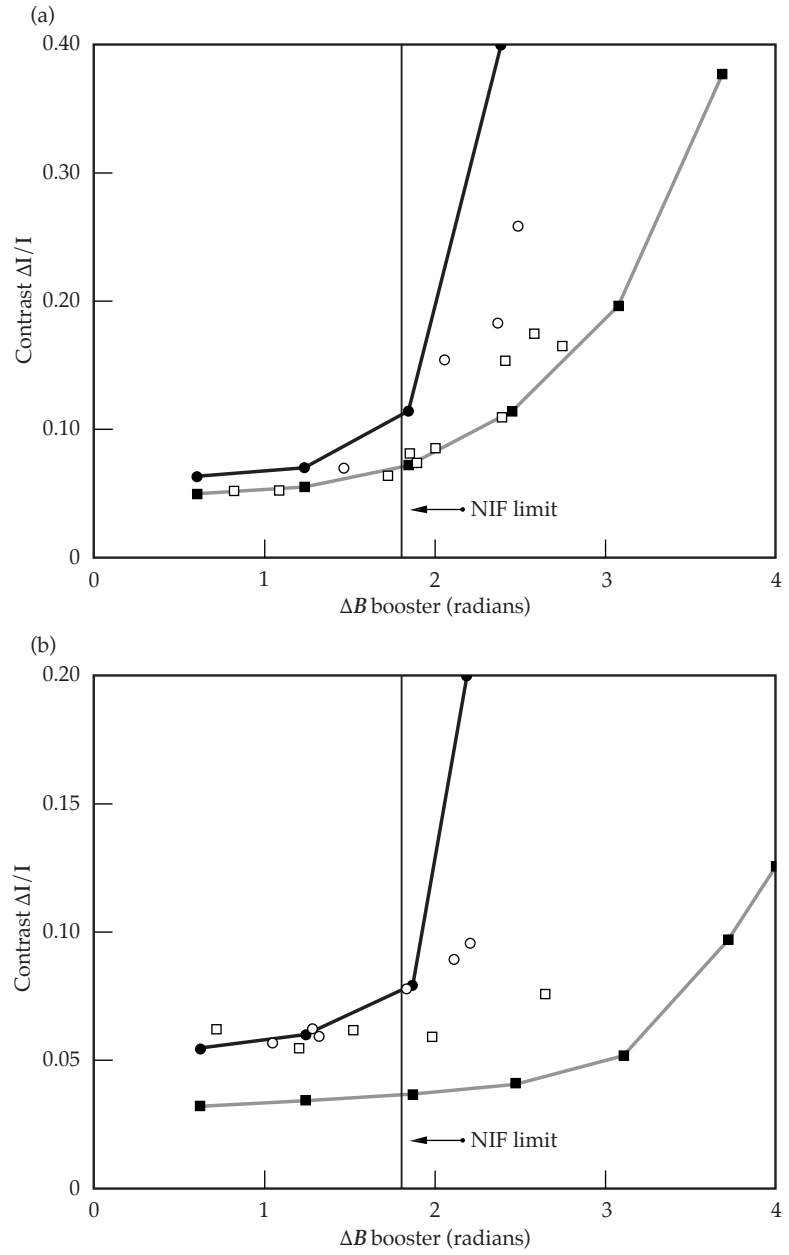


FIGURE 2. 1ω near-field beam modulation at (a) low and (b) high B -integral through the booster amplifiers. Images show the central 24.4 cm of the beam and were obtained with output sensor looking through the transport spatial filter with the pinhole removed. (70-00-0499-0781pb01)

High-Energy Shaped Pulses for ICF

Temporal pulse shaping will be achieved on the NIF using low-voltage waveguide electrooptic modulation techniques in integrated optical circuits.⁸ This technology has been used on Beamlet to produce 20-ns, NIF-like ignition pulses with a pulse-shaping system consisting of two arbitrary waveform generators (AWGs) in series. A 20-ns AWG with 1-ns resolution formed the electrical signal corresponding to the long,

FIGURE 3. (a) Near-field irradiance contrast ratio vs B -integral for two cavity/transport pinhole configurations: 130 μrad /open (squares) and 200 μrad /open (circles). Measurements and simulations are denoted by open and filled symbols, respectively. (b) Results obtained with a pinhole in the transport spatial filter: 130 μrad /100 μrad (squares) and 200 μrad /200 μrad (circles). (70-00-0499-0782pb01)



low-intensity foot of the pulse, and a 7-ns fast (250-ps) AWG appended the high-bandwidth features of the complex pulse shape to the end of the foot. The resulting driver voltage signal controlled the light amplitude propagated through a LiNbO_3 modulator.

The required optical pulse shape at the modulator was calculated from the desired pulse shape at the laser output using empirical lumped-gain models for the various Beamlet amplification stages. The relatively small amount of saturation in the

regenerative amplifier and preamplifier was well approximated by energy gains G that decreased linearly with extracted energy at the rate of 1.4%/mJ and 16%/J, respectively. The gain model for the main amplifier was based on the curve fit to the data shown in Figure 4, which plots measured input energy vs output energy for shots spanning approximately one year. The data was best approximated with two polynomials: 2nd order below 6583 J and 3rd order above. The resulting composite curve produces a better fit than could be

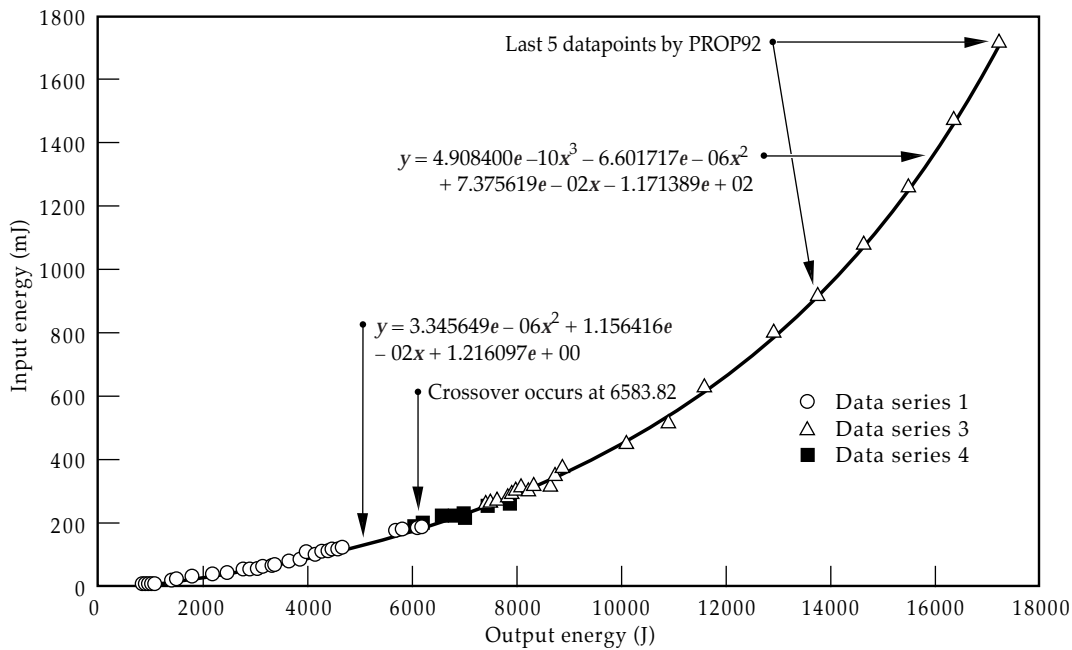


FIGURE 4. Gain of the main amplifier plotted as input energy required to produce a given output energy. Curve denotes best fit used for pulse shaping. (70-00-0499-0783pb01)

achieved with a simple single-gain-element Frantz–Nodvik calculation, and has proven adequate for pulse shaping.

With predictions based on these models, we produced the 15.5-kJ, 1ω NIF ignition pulse shown in Figure 5. Scaled for beam size, the energy and peak power of this pulse fall on the NIF red-line performance curve for square pulses shown in Figure 6, demonstrating the primary $1.05\text{-}\mu\text{m}$ laser requirement for inertial confinement fusion. Successful propagation of this pulse required advances in spatial filtering, described in the following section.

Spatial Filtering

Spatial filter issues of importance for the NIF fall into three categories:

1. Pinhole closure—the problem of keeping the required small pinholes open for the full duration of the NIF ignition pulse.
2. Back reflections—the need to avoid back reflections from pinholes that can damage the injection optics.
3. Background pressure—the question of maximum safe operating pressures for NIF cavity and transport spatial filters (CSFs and TSFs, respectively).

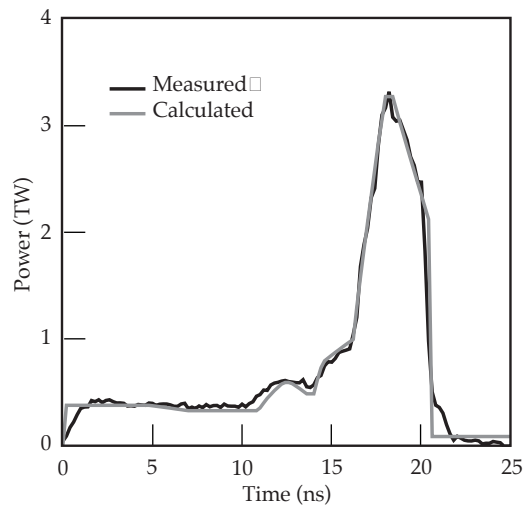


FIGURE 5. Measured temporal profile of a 15.5-kJ, 1ω ignition pulse produced on Beamlet. Data is in good agreement with predictions based on the pulse shaping model (gray profile). (70-00-0499-0784pb01)

Beamlet experiments addressed each of these areas in turn.

Pinhole Closure

Three types of pinholes were tested for closure on Beamlet, as shown in Figure 7. The first type is a washer design consisting of a hole in a flat plate oriented at approximately normal incidence to the beam. The second type is a leaf design consisting of four azimuthal segments displaced along

FIGURE 6. NIF 11-5 amplifier configuration safe performance limit, with Beamlet experimental data points scaled to the NIF beam area. Square pulse data is plotted as open circles. Shaped pulse data (filled circles) is characterized by an equivalent pulse duration defined as the energy divided by peak power.
(70-00-0499-0785pb01)

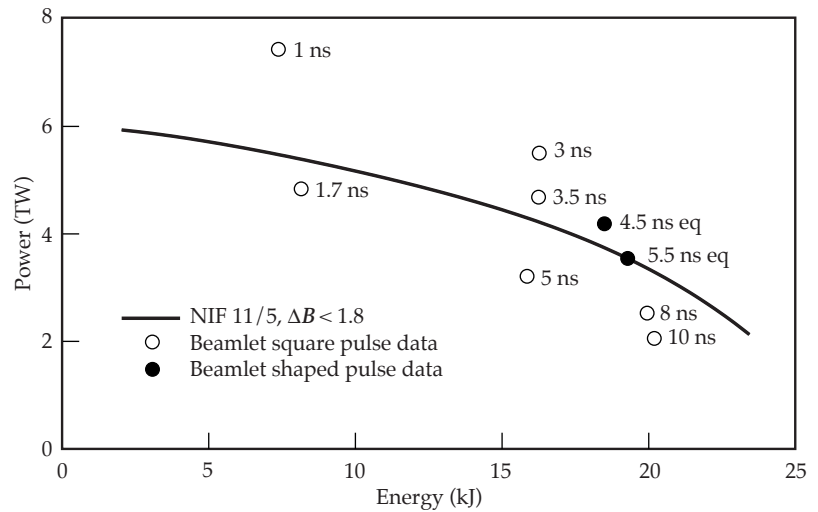
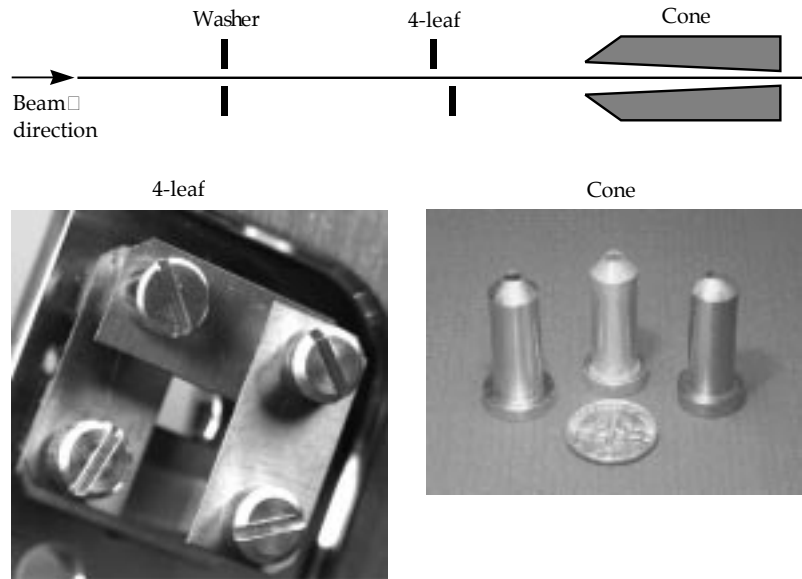


FIGURE 7. The three types of pinholes tested on Beamlet.
(70-00-0499-0786pb01)



the beam axis to eliminate the possibility of plasma convergence at the center of the pinhole. The third type is a conical pinhole, designed such that low-density plasmas on the surfaces reflect or refract the incoming light rather than absorb it.⁹ The design of the cone pinhole is parameterized by the cone angle α and the cone length L . For the Beamlet tests we set $\alpha = 1.3 \alpha_{\min}$ and $L = 0.7L_{\max}$, where α_{\min} equals the f -number of the spatial filter divided by 2 and $L_{\max} = 2R_0/(\alpha + \alpha_{\min})$.¹⁰ Here R_0 is the radius of the pinhole aperture, which when divided by the focal length of the spatial filter input lens gives the cutoff angle of the pinhole.

Pinhole performance was evaluated with a specialized set of diagnostics. A pulsed Mach-Zender interferometer was used to measure the phase shift of a 532-nm probe beam passing through the pinhole during the passage of the main laser pulse. The fringe pattern from the interferometer was recorded on a streak camera and a 120-ps rise-time gated optical imager to obtain time-resolved phase maps in x - t and x - y that could be correlated with electron density in the pinhole (see Reference 11 and article by Feit on p. 63 of this *Quarterly Report*). A second gated optical imager measured the transmitted near-field beam

irradiance during the last nanosecond of the pulse. Because pinhole closure affects the trailing edge of the pulse first, this diagnostic gave the most definitive indication of closure at near-threshold conditions. A second streak camera was configured to image a central strip of the transmitted near-field beam irradiance and measure the time variation of the modulation in that strip. This diagnostic was used to determine when the increased modulation associated with closure occurred during the pulse.

The majority of the tests were conducted with 20-ns square pulses to simulate the leading foot of a shaped ignition pulse. To compare shots of different energies E_{pulse} and closure times t , we adopted a figure of merit E_{closure} defined as the energy needed to close a pinhole at the end of a 20-ns square pulse. Because the closure time is inversely proportional to the plasma expansion velocity, which in turn is proportional to the laser irradiance at the edge of the pinhole,¹¹ E_{closure} is simply $E_{\text{pulse}}t(\text{ns})/20$, the validity of which has been confirmed by measurement. Applying this analysis to the test data for $\pm 100\text{-}\mu\text{rad}$ pinholes with 20-ns square pulses yields the results summarized in Figure 8, which plots E_{closure} as a function of atomic mass for the three pinhole types and four different materials. Conical pinholes outperformed washer and four-leaf pinholes in all cases. In general, performance

was also better for higher-Z pinholes which produce shower closure velocities, with the exception of the Au cone, which did not perform as well as the Ta cone. It is believed that an inadequate finish on the interior surface of the Au cone caused its lower-than-expected performance.

The conical pinhole design was also tested using 20-ns shaped ignition pulses. The required ignition pulse at the input to the NIF frequency converter has an energy of 19.4 kJ and a contrast of 10:1 (Figure 5). However, simple scaling laws for pinhole closure show that the pinhole most susceptible to closure is not the output pinhole in the $f/80$ TSF, but the Pass-4 pinhole in the $f/31$ CSF, where the pulse energy is 14.8 kJ and the contrast is 21:1. Tests with this pulse shape closed a $\pm 100\text{-}\mu\text{rad}$ stainless-steel (SS) cone pinhole at $3\times$ the energy of the corresponding 20-ns foot-only pulse, suggesting that the closure energy for ignition pulses can be obtained by multiplying E_{closure} in Figure 8 by 3. In this case, none of the $\pm 100\text{-}\mu\text{rad}$ pinholes tested would work for the NIF ignition pulse. The $\pm 100\text{-}\mu\text{rad}$ Ta cone comes close based on this simple $3\times$ scaling, but additional margin would be needed for the increased angular divergence associated with beam smoothing by spectral dispersion (SSD) and for finite alignment tolerances.

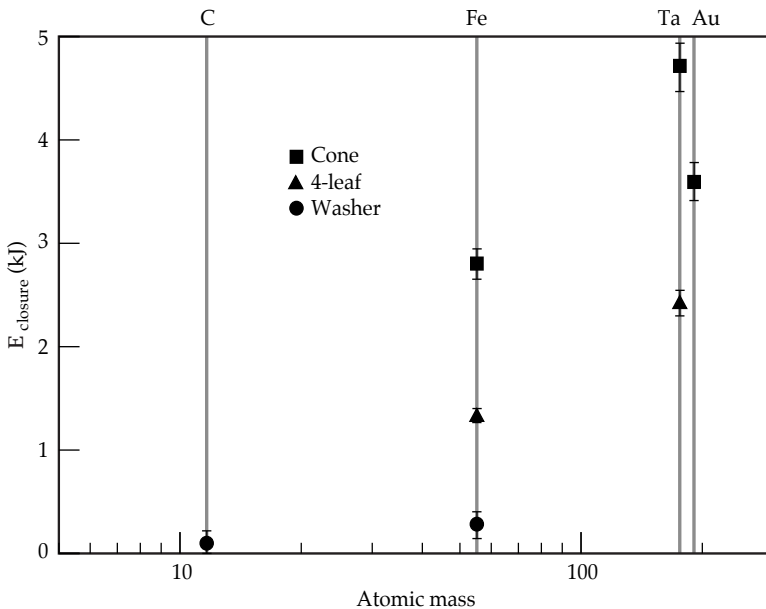


FIGURE 8. Closure energies for three types of $\pm 100\text{-}\mu\text{rad}$ pinholes plotted vs atomic mass. (70-00-0499-0787pb01)

On the other hand, a $\pm 150\text{-}\mu\text{rad}$ SS cone pinhole meets NIF requirements with ease, passing a 15.5-kJ, 10:1 ignition pulse with $\pm 7.5\text{ }\mu\text{rad}$ of added SSD divergence with no sign of closure. The 10:1 ignition pulse is harder to keep open than the required 21:1 pulse with the same total energy because the intensity in the foot is larger by 2 \times . Figure 9 shows the interferometry data for this shot. The interferogram recorded by the streak camera is shown on the left. Analysis of the fringe pattern at the time indicated gives the phase shift of the probe pulse as a function of position in the pinhole, plotted on the right. A second curve in this plot shows how the phase shift would look at closure based on data from a different shot. The large separation between the curves indicates that the $\pm 150\text{-}\mu\text{rad}$ SS cone pinhole was quite far from closure at end of the pulse. This pinhole is currently our baseline choice for NIF.

Back Reflections from Pinholes

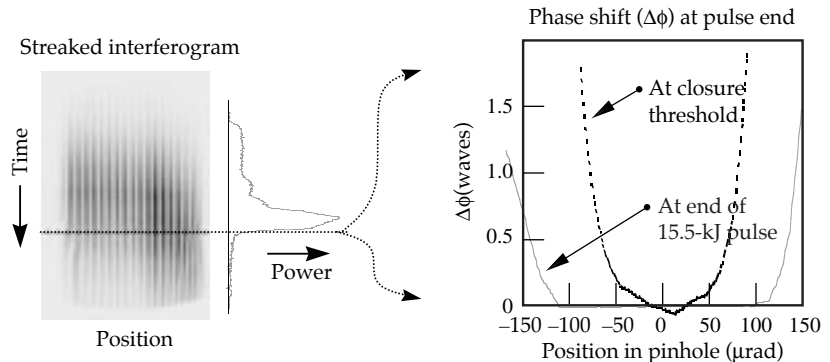
Back reflections have been a problem for staged pinhole geometries, in which the pinhole angular acceptance is gradually decreased from the input to the output of the laser. Because pinhole staging results in the best output beam quality, it remains the preferred mode of operation, and thus a solution for back reflections is required. All of the pinhole tests were performed in this configuration and generated measurable back reflections for pulses greater than about 1 TW into the transport spatial filter. However, the energy reflected

from the cone pinholes was down by at least an order of magnitude from the energy reflected by the other pinhole geometries. Furthermore, its back reflection increased approximately linearly with power, whereas the back reflection for both leaf and washer pinholes increased nonlinearly, indicating a stimulated scattering process at the pinhole. Imaging of the back-reflected light (Figure 10) showed unambiguously that the back reflections originate from the surfaces of the pinhole rather than from an on-axis plasma, confirming the advantages of the cone geometry over the planar washer and leaf designs.

Maximum Background Gas Pressure

Residual gas in the spatial filters at pressures above a certain maximum p_{th} causes increased modulation in the near-field irradiance of the transmitted pulse, similar to the modulation observed above the threshold for pinhole closure. Threshold pressure is known to depend strongly on spatial filter f -number,¹² and as a result the Beamlet gas-pressure tests were conducted with both $f/26$ and $f/78$ geometries to determine values for p_{th} applicable to the NIF CSF ($f/31$) and TSF ($f/80$), respectively. Figure 11 shows the results plotted as pressure vs peak intensity at the focus of the spatial filter. Three types of points are plotted for each f -number to distinguish whether the data came in above, at, or below p_{th} as gauged by the modulation level in the transmitted near-field beam irradiance. Best-fit p_{th} for the $f/26$ data is indicated by the upper curve,

FIGURE 9. Interferometric data showing the phase shift of a probe pulse at the pinhole during passage of a 15.5-kJ, 10:1 contrast ignition pulse with $\pm 7.5\text{ }\mu\text{rad}$ of added SSD divergence. The pinhole was a $\pm 150\text{-}\mu\text{rad}$ SS cone. (70-00-0499-0788pb01)



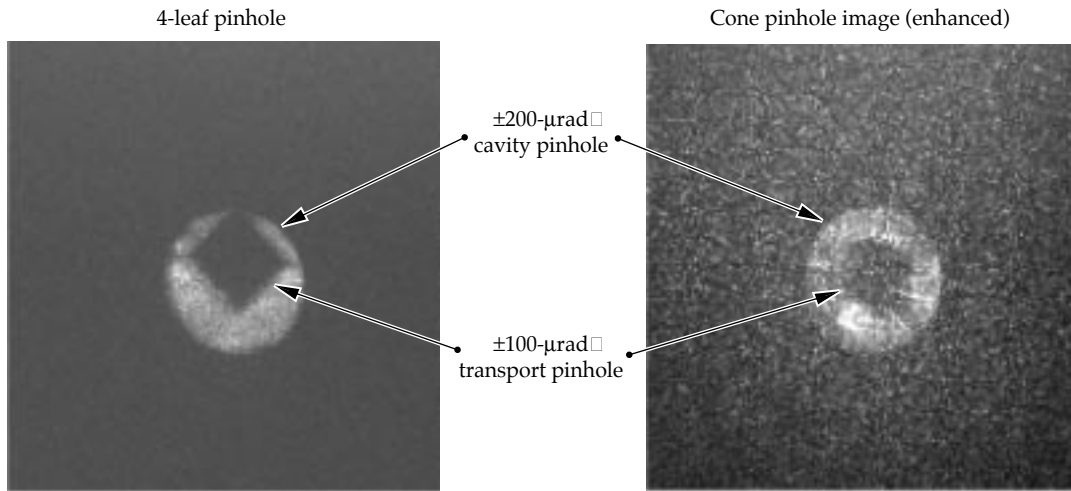


FIGURE 10. Back-reflected laser light from TSF pinholes, as imaged through the pinholes in the CSF. Back-reflected energy from the 4-leaf pinhole was 180 mJ at 2.0 TW, as measured at the input sensor, while that from the cone was only 10 mJ at 3.5 TW. (70-00-0499-0789pb01)

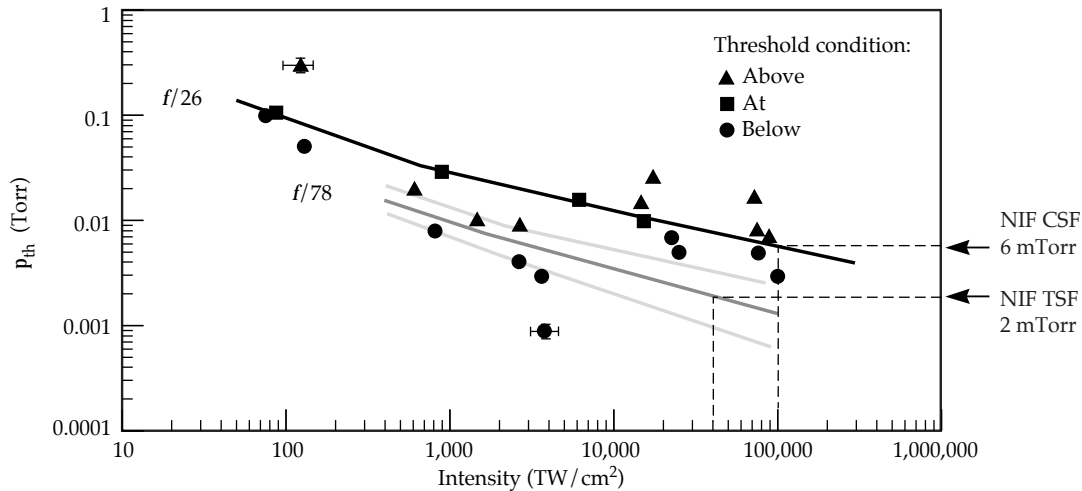


FIGURE 11. Data for determining threshold pressure p_{th} , at which residual spatial filter pressure disturbs the transmitted pulse. Filled triangles and squares denote data that was above or at threshold, respectively. Data below threshold is indicated by circles. Dashed lines show predicted thresholds at expected NIF filter intensities (70-00-0499-0790pb01)

which is well defined out to the maximum intensity expected for the NIF CSF. The $f/78$ data, however, was obtained by reducing the aperture of the beam by $3\times$, which also reduced the maximum power output by $9\times$. Consequently, the $f/78$ data ends well short of the expected intensities for the NIF TSF. Maximum and minimum credible extrapolations are indicated by the two gray curves, with the dark gray intermediary curve corresponding to our current best estimate. The results give p_{th} values of 6 mTorr for the NIF CSF and 2 mTorr for the TSF. There is roughly a factor of two uncertainty in the $f/78$ data, because the beam quality was significantly

better for the central subaperture of the beam used in those tests, and better beam quality has been observed to give lower values of p_{th} . Safety considerations dictate that the maximum allowed NIF operating pressures be roughly an order of magnitude below these values.

Measurements with both residual gas and a pinhole in the spatial filter showed no interaction between the effects of the residual gas and pinhole closure. $E_{closure}$ remains essentially constant for pressures from well below to $3\times$ above p_{th} . The reason there is no interaction is that the two phenomena affect different temporal parts of the pulse. Data from the streaked near-field diagnostic

showed that pressures at or slightly above p_{th} affect mainly the leading edge of the pulse, whereas near-threshold pinhole closure affects the trailing edge.

Wavefront Control and Beam Focusability

Effective wavefront control is essential for achieving the high-brightness focal-spot conditions specified for NIF targets. For example, certain NIF weapons physics target requirements call for delivery of 500 TW of 3ω radiation inside a $250\text{-}\mu\text{m}$ -diam focal spot.¹³ For the 7.7-m focal-length lenses on the NIF target chamber, this spot size corresponds to a half angle of $16\text{ }\mu\text{rad}$, which sets a stringent upper limit for the divergence of the laser.

There are several sources of divergence in the laser, primarily in the 1ω section, that can significantly degrade the quality of the focal spot unless mitigated or otherwise controlled. These sources fall readily into four categories:

1. Static phase errors related to the finishing, mounting, and alignment of the optical components.
2. Prompt phase errors related to a deformation of the amplifier slabs during pumping.¹⁴
3. Thermally induced phase errors related to heat accumulation in the amplifiers, including gas turbulence effects.^{15,16}
4. Nonlinear phase errors associated with the intensity-dependent ripple growth and whole-beam self-focusing.

At a given power level, minimum divergence and maximum beam brightness are achieved when the system is cold and thermally induced phase errors are absent (see Figure 12). In this case, performance is primarily limited by the fraction of prompt and static phase errors that remain uncorrected by the wavefront-control adaptive optic system (AOS) as a result of its limited spatial resolution.

The active component in the Beamlet AOS is a 7-cm-square deformable mirror

(DFM) with 39 independent actuators;¹⁷ the number of actuators and their arrangement is similar in design to the 40-cm mirror that will be deployed on the NIF.¹⁸ The mirror resides at the output of the preamplifier (see Figure 1) and conditions the wavefront of the pulse before it is injected into the cavity amplifier. Wavefront data for closed-loop control of the mirror is provided by either of two 77-element Hartmann sensors located in diagnostic packages situated at the input and output of the main amplifier. Closed-loop control allows the figure of the mirror to be updated continuously ($\sim 1\text{ Hz}$ response) to maintain a predefined wavefront at the Hartmann sensor, which is typically specified to be either “flat” or a compensating figure determined from the wavefront error measured on a previous shot (termed “prefigure”). Additional diagnostics, including radial shear interferometers, were used to independently check the operation of the AOS and quantify beam quality.¹⁹ Measurements of system

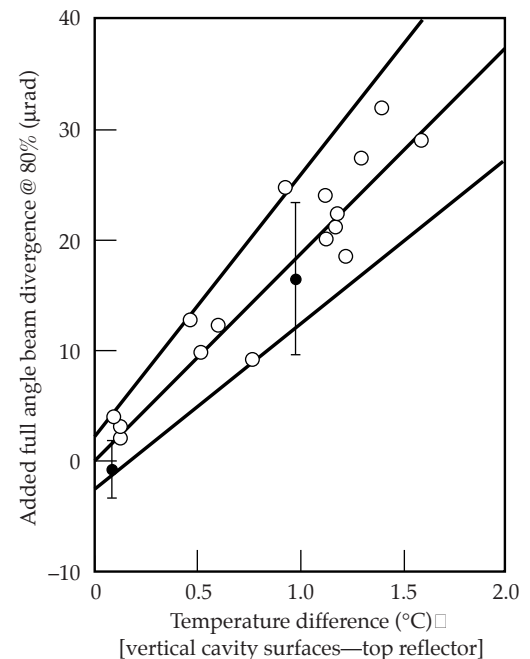


FIGURE 12. Beamlet measurements correlating 1ω laser divergence with amplifier temperature. The AOS is unable to correct for gas-density fluctuations of high spatial frequency caused by amplifier heating. (02-30-1093-3491pb01)

wavefront and beam quality both with and without an optimized AOS are presented in the following subsections.

Preamplifier Wavefront Quality

The output of the Beamlet preamplifier is very close to diffraction-limited. Continuous-wave measurements showed that the AOS improves the wavefront of the preamplifier by ~ 0.25 waves to achieve a residual error of 0.32 waves peak to valley, 0.06 waves rms, and a Strehl ratio of 0.87. Firing the 5-cm rod added ~ 0.2 waves of prompt phase error that was not readily evident unless the AOS was actively correcting the static error. With the rod pumped, wavefront measured with and without the DFM was qualitatively different but similar in peak-to-valley and rms error. The 80% spot size was equivalent for the two cases ($4.3\text{-}\mu\text{rad}$ half angle), but the DFM improved the brightness of the focal spot by $\sim 30\%$. These results are consistent with those of Reference 20.

Output Wavefront Quality

Beam quality at the output of the system is approximately $2.5\times$ the diffraction limit with the AOS optimized to correct both prompt and static wavefront errors in the main amplifier, meaning that 80% of the energy is in a diameter $2.5\times$ the 80% diameter of a diffraction-limited beam. With the preamplifier pumped and the main amplifiers static (rod shot condition), the residual wavefront error at the output of the system was ~ 1 wave peak to valley, 0.2 waves rms, and the 80% half angle of the focal spot was $10.5\text{ }\mu\text{rad}$ (Figure 13a). The measurement was made with the AOS operating closed-loop to maintain a flat wavefront at the output Hartmann sensor up until 1 s prior to the shot. Data obtained under similar conditions, but with the main amplifiers pumped, yielded an output wavefront error of ~ 3 waves peak to valley, 0.6 waves rms, and a much-degraded focal spot (Figure 13b). The difference between these two wavefronts gives the prompt distortion caused by

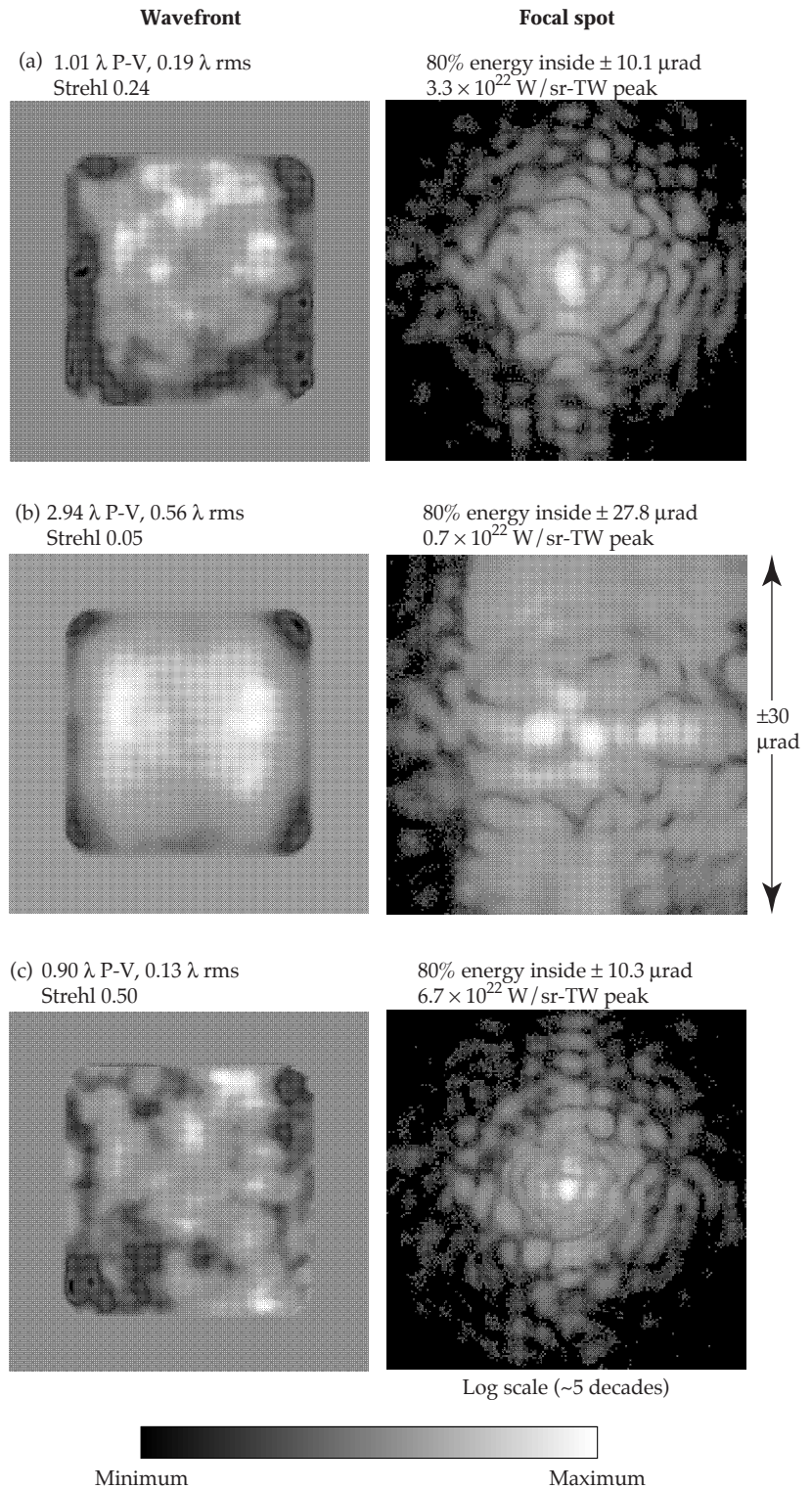


FIGURE 13. 1 ω wavefront and focal spot measured at the output of the main amplifier for (a) rod shot with the AOS maintaining a flat wavefront up until 1 s prior to the shot, (b) same AOS condition as (a) but with the main amplifiers pumped, and (c) main amplifiers pumped with the AOS maintaining an optimized prefigured wavefront up until 1 s prior to the shot. (70-00-0499-0791pb01)

pumping the large amplifiers. With an appropriate prefigure of the DFM based on this measurement, it was possible to achieve an output wavefront and focal spot on a low-power system shot that were equivalent in quality to the data obtained on rod shots (Figure 13c).

These results demonstrate that the 39-actuator design of the DFM is highly effective at correcting the prompt wavefront distortions incurred in the main amplifier, and that, as a result, the focusability of the laser is primarily limited by the static errors in the main amplifier that are not correctable with the AOS. In the case of Beamlet, this residual error has been shown to meet the NIF high-brightness focal-spot requirements at both low and high power. Table 1 summarizes the results of high-power focal spot measurements conducted with an optimized AOS at output powers of up to 5.3 TW (1ω) and 3.1 TW (3ω) in a 200-ps pulse. Amplifier configuration is denoted 11-0 or 11-5, depending on whether the booster amplifier was pumped. Maximum power was achieved with the 11-5 configuration, for which the total B -integral accumulated in the amplifiers was 2.6 rad (ΣB), and the corresponding 80% power half angles of the 1ω and 3ω focal spots were 12 and 15 μrad , respectively. Scaling the power in the 3ω focal spot (0.8×3.1 TW) by the

ratio of NIF to Beamlet beam sizes ($1240\text{ cm}^2/1050\text{ cm}^2$) and multiplying by the number of beams (192) and the transmission of the final optics (0.94) results in a NIF-equivalent performance of 540 TW inside $\pm 15\text{ }\mu\text{rad}$. Thus if the quality and associated static errors of the NIF optics are held to Beamlet levels, and the NIF AOS behaves equivalently, the NIF focusing requirements will be achievable.

Static Errors and Optics Finishing Specifications

The static wavefront errors in the Beamlet amplifier were quantified by calculating the difference between the input and output wavefronts, as measured on a rod shot with a flat mirror in place of the DFM. The result, shown in Figure 14, has proven useful for correlating optics-finishing specifications with focal-spot performance. For the central core of the focal spot, corresponding to divergence angles less than $\sim 30\text{ }\mu\text{rad}$, the finishing effects of importance are long-wavelength figure errors, for which the appropriate specification is the rms gradient of the transmitted wavefront.²¹ Applying a low-pass filter with a cutoff frequency of 0.03 mm^{-1} to the difference data in the figure and calculating the rms gradient of the result yields a value of $1300\text{ }\text{\AA}/\text{cm}$ for all

TABLE 1. Results of high-power focal spot measurements conducted with an optimized AOS at output powers of up to 5.3 TW (1ω) and 3.1 TW (3ω) in a 200-ps pulse.

Shot	Amplifier	$\Sigma B_{1\omega}$ (rad)	$P_{1\omega}$ (TW)	$P_{3\omega}$ (TW)	1 ω focal spot			3 ω focal spot		
					50% half angle (μrad)	80% half angle (μrad)	Peak intensity*	50% half angle (μrad)	80% half angle (μrad)	Peak intensity*
B7082005	11-0	1.3	1.3	0.6	5.4	11.7	3.7	8.0	13.6	0.67
B7082103	11-0	2.0	2.0	1.2	5.4	11.5	3.9	7.4	12.8	0.73
B7082205	11-0	2.1	2.2	1.3	5.7	11.8	3.0	8.1	13.7	0.70
B7082501	11-0	2.8	2.8	1.8	5.1	11.6	3.8	8.4	14.1	0.67
B7082601	11-5	1.6	3.4	2.3	5.3	12.3	3.3	7.7	12.5	0.92
B7082702	11-5	1.8	3.8	2.2	4.6	11.7	3.9	6.7	12.3	0.83
B7082802	11-5	2.6	5.3	3.1	4.4	12.1	4.7	6.5	14.9	0.82
B7082902	11-5	2.4	5.0	3.2	4.0	11.6	4.8	7.3	15.4	0.77

* 10^{22} W/sr-TW . Divide by the square of the lens focal length in cm to obtain irradiance ($\text{W}/\text{cm}^2\text{-TW}$)

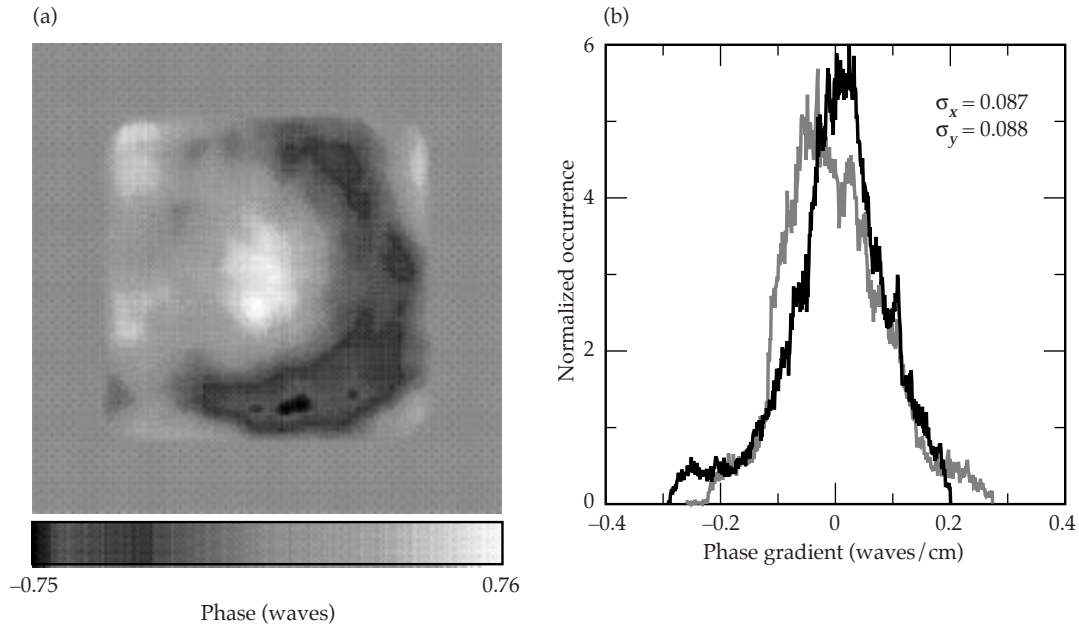


FIGURE 14. (a) Static wavefront distortion of the main amplifier, measuring 1.51λ P-V, 0.34λ rms. (b) Horizontal (gray) and vertical (solid) gradient distributions after filtering with a cutoff frequency of 0.03 mm^{-1} . Total rms gradient is the rss of σ_x and σ_y . (70-00-0499-0792pb01)

of the optics combined. Assuming incoherent addition of phase between different elements, and accounting for multiple coherent passes through sections of the amplifier, the average rms gradient per optic is estimated to be $1300/17.2 = 75 \text{ Å/cm}$. Simulations using an average gradient distribution based on this result, and nominal power spectral densities for the high-frequency aberrations²² predict focal spots that are consistent with the Beamlet measurements.²³ Thus, to ensure focal-spot performance equivalent to Beamlet, specifications for NIF optics currently limit the rms gradient of the transmitted wavefront to 70 Å/cm for spatial scale lengths $>33 \text{ mm}$.

Final Optics and Frequency Conversion

The NIF final optics perform several critical functions in a compact assembly:

1. Frequency converting the 1ω pulse from the laser amplifier to 3ω with high efficiency.
2. Focusing the 3ω energy onto the target.
3. Diverting the unconverted energy away from the target.
4. Providing a full-aperture sample of the 3ω beam for diagnostics.

5. Randomizing the spatial coherence of the laser energy at the target.
6. Shielding upstream optics from debris and high-energy x rays and neutrons emitted from the target.

The designs of the components that accomplish these tasks have been described elsewhere.^{24,25}

To test and validate various aspects of the final optics design on Beamlet, we constructed a “test mule” (term borrowed from the auto industry describing a flexible prototype) at the output of the main laser amplifier that allowed us to field 37-cm-aperture versions of the optical components in a NIF-like configuration without the cost and complexity of activating a complete final optics assembly (FOA). A NIF-like 1ω window at the input to the test mule isolated the vacuum environment of the final optics from the main amplifier, allowing safe operation at full 3ω fluence without risk of damage and potential fracture of the input window. Temperature-controlled water flowing through heat exchangers on the surface of the test mule maintained a constant thermal environment of $20.0 \pm 0.1^\circ\text{C}$ for the frequency converter; similar passive cooling will be used for the NIF FOA. Beam alignment into the test mule and the 3ω diagnostics package was accomplished

using four 45° high-damage threshold 1 ω mirrors. The requirement for slight out-of-plane orientation of the mirrors resulted in mixed “s” and “p” reflections and the associated risk of beam depolarization, which could negatively impact frequency conversion. Fractional depolarized energy was measured both with and without the mirrors and found to be acceptable at less than 1%. Test mule experiments addressing frequency conversion and high-fluence operation of the final optics are described in the following subsections.

Frequency Conversion

Experiments conducted with the test mule played an important role in proving the design of the NIF frequency converter and validating the physics model on which a detailed error analysis of its performance is based. The model is the most comprehensive yet developed for the converter, including details such as spatially

varying birefringence in the crystals that has only recently been quantified using orthogonal polarization interferometry techniques.²⁶ Several Beamlet test configurations, summarized in Table 2, were used to evaluate both second-harmonic generation (SHG) and third-harmonic generation (THG), with converters consisting of both conventionally grown and rapidly grown potassium dihydrogen phosphate/potassium dideuterium phosphate (KDP/KD*P) crystals.²⁷ The crystals were tested in a prototype 37-cm-aperture final optics cell (FOC), which also contained the final focus lens, as shown in Figure 15a. Precision-machined surfaces in the FOC supported the optics around their perimeter and registered them with microradian tolerance. Compliant clamps held the optics in place; a load of 0.6 lb/in. was found to adequately constrain the crystals while providing good surface figure (Figure 15b). The configuration of the 1 ω laser was the same for all tests: eleven cavity amplifiers, five booster amplifiers, a 200- μ rad C pinhole in the Pass-4 cavity spatial filter pinhole, and a 150- μ rad SS cone pinhole in the transport filter. Pulse format was 1.5 ns square. Estimated accuracy of the energy-conversion efficiency measurements was $\pm 6\%$ (3 σ).

SHG efficiencies measured with a conventionally grown Type-I doubler from a NIF production boule are plotted in Figure 16a. Maximum energy efficiency was 73% (aperture-averaged, time-integrated) at an input 1 ω irradiance of approximately 4 GW/cm² (aperture-averaged, peak-in-time). Similar tests of a rapidly grown Type-I doubler achieved 70.5% efficiency at similar drive irradiance. The measured performance of these crystals was in good agreement with modeling based on measured 1 ω pulse parameters and measured crystal refractive-index variations. The effects of the latter were verified by measuring the 2 ω near-field fluence distributions with the crystal tilt biased well away from exact phase matching, a configuration very sensitive to phase mismatch. As shown in Figure 17, the resulting nonuniformities in the data were well reproduced in the model.

THG efficiencies measured with a rapidly grown doubler and tripler are plotted in Figure 16b. Maximum energy

Table 2. Beamlet test configurations used to evaluate both SHG and THG, with converters consisting of both conventionally grown and rapidly grown KDP/KD*P crystals.

Parameter	Conventional		Rapid growth	
	SHG	THG	SHG	THG
1 ω laser				
Beam size (cm)	34	34	34	30
Doubler				
Serial number	345-1	345-1	RG8B-2	RG8B-2
Thickness (mm)	11.09	11.09	11.10	11.10
$\Delta\theta$ distribution (μ rad int, 1 σ)	22.3	18.8	17.5	27.8
Surface loss (% before/after)				
S ₁ (1 ω)	0.91/–	–/1.49	1.03/–	1.64/1.67
S ₂ (1 ω)	0.91/–	–/1.49	1.03/–	1.64/1.67
S ₂ (2 ω)	1.70/–	–/2.53	1.48/–	2.85/3.30
Tripler				
Serial number	–	LL1-37-1	–	RG8A-1
Thickness (mm)	–	9.48	–	9.41
Deuteration level (%)	–	70	–	85
$\Delta\theta$ distribution (μ rad int, 1 σ)	–	36.2	–	67.7
Surface loss (% before/after)				
S ₁ (1 ω)	–	0.60/–	–	2.75/3.05
S ₁ (2 ω)	–	1.82/–	–	1.30/2.20
S ₂ (3 ω)	–	0.10/–	–	0.37/2.21
Measured performance				
Maximum energy efficiency	73	75	70.5	73.5
At 1 ω irradiance (GW/cm ²)	4.0	3.8	3.9	3.6

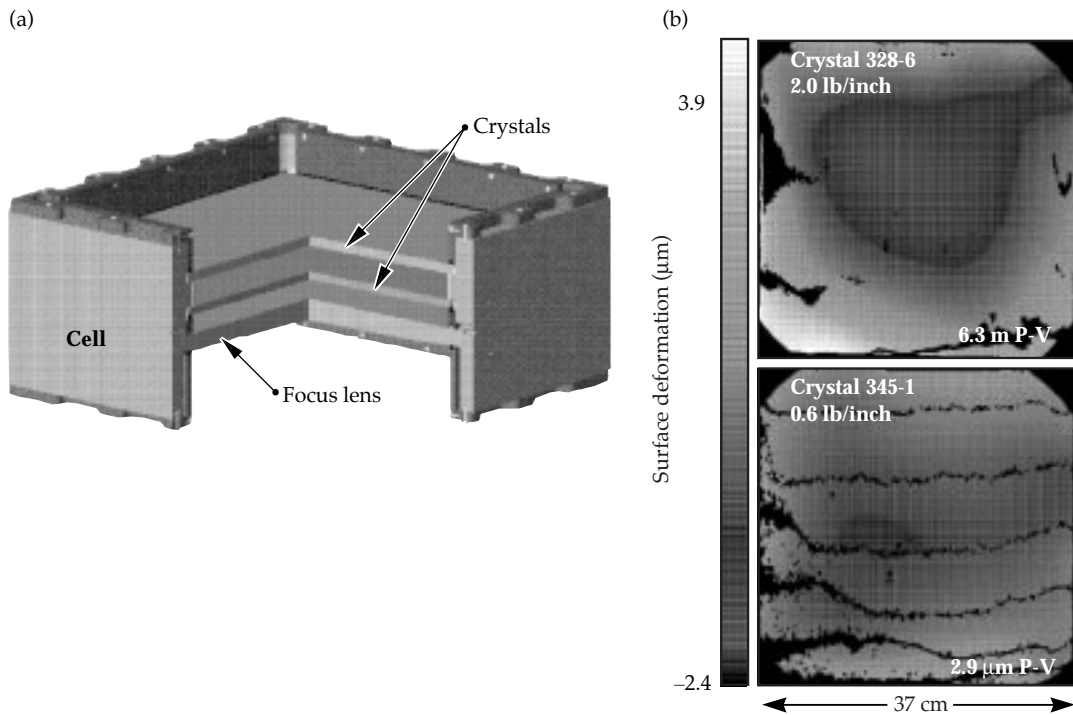


FIGURE 15. (a) Cut-away view of the final optics cell showing mounting scheme for the crystal and focus lens. (b) Measured surface figure of a mounted doubling crystal. Dark bands are caused by interference of the reflections from the near-parallel front and back surfaces of the crystal. (70-00-0499-0793pb01)

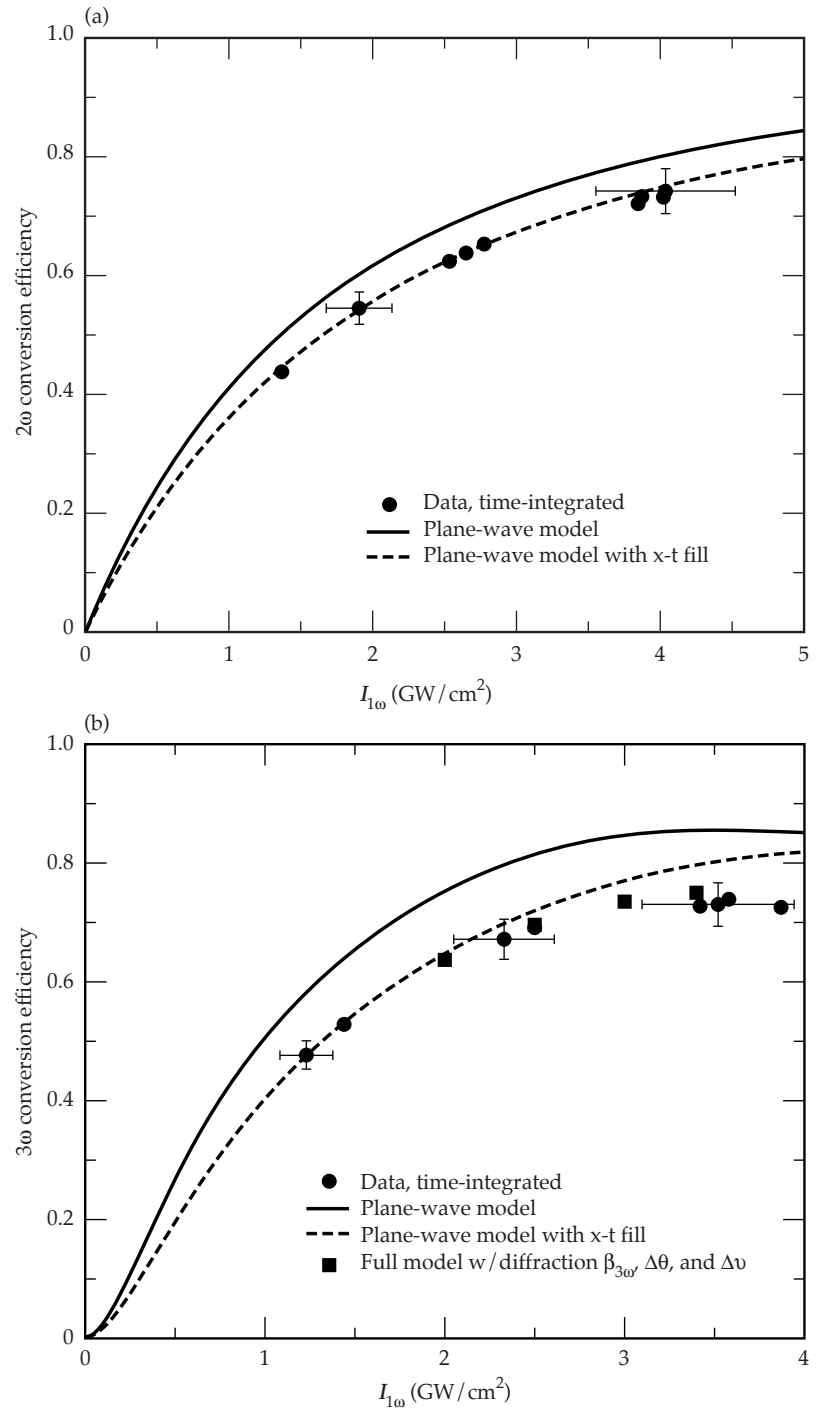
efficiency was 73.5% at an input 1ω irradiance of approximately 3.6 GW/cm^2 . In comparison, the model, with an input field based on near-field 1ω irradiance data and an eleven-time-slice approximation of the measured 1ω pulse shape, predicted an energy conversion efficiency of 77%, and a peak-power conversion efficiency of 79.5%. Including the 30-GHz bandwidth of the drive pulse and the measured depolarization in the Beamlet laser lowers the calculated energy efficiency to 75%. Incorporating the additional losses caused by the degradation of the sol-gel antireflection coatings over the course of the experiment further reduces the efficiency to 71.5%, suggesting that the model is accurate to within the uncertainty in the component transmissions. Calculated and measured near-field fluence distributions for both the third-harmonic and residual second-harmonic fields were in fairly good agreement as a result of having the orthogonal-polarization interferometry data incorporated in the model. The energy balance in the model (the ratio of total energy out of the converter to total energy into the converter) was $\sim 3\%$ higher than observed, consistent with the actual transmissions of the components in vacuum

being lower than the initial values modeled. Based on these results, peak-power 3ω conversion efficiencies approaching 80% should be achievable at NIF ICF drive irradiances, provided that high-quality antireflection coatings are maintained on the frequency-converter optics.

High-Fluence Operation

High-energy operation of the final optics was investigated as high-damage-threshold fused-silica components became available. Third-harmonic fluences of up to 8 J/cm^2 and NIF-equivalent energies of up to 9.6 kJ in 3-ns square pulses were tested in a series of three campaigns (Figure 18) that produced valuable data for extrapolating component performance and lifetime for the NIF.²⁸ The tests culminated in a limited number of full-fluence shots through an integrated final optics configuration, including frequency-conversion crystals, focus lens, and a diffractive optics package containing a color separation grating (CSG) and beam sampling grating (BSG) on a single silica plate, a kinoform phase plate (KPP), and a debris shield. Time constraints imposed by Beamlet shutdown allowed

FIGURE 16. (a) Plot comparing measured and calculated SHG efficiency versus 1ω irradiance for conventional-growth doubler #345-1. (b) Comparison of measured and calculated THG efficiency for rapid-growth doubler #RG8B-2 and tripler #RG8A-1. (70-00-0499-0794pb01)



very little on-line characterization of the individual diffractive optics prior to the integrated test. A low-damage-threshold version of the KPP was tested previously and its performance reported elsewhere.²⁹ The CSG concept was used successfully at low fluence in an experiment conducted for the French Commissariat à l'Energie Atomique. Results

of the high-fluence tests revealed problems with CSG-induced beam modulation problems and damage associated with the sol-gel coating being thicker than $\lambda/4$ near the step edges, an effect previously identified as being responsible for reducing CSG diffraction efficiency. Improved CSG designs under development are expected to eliminate this problem.

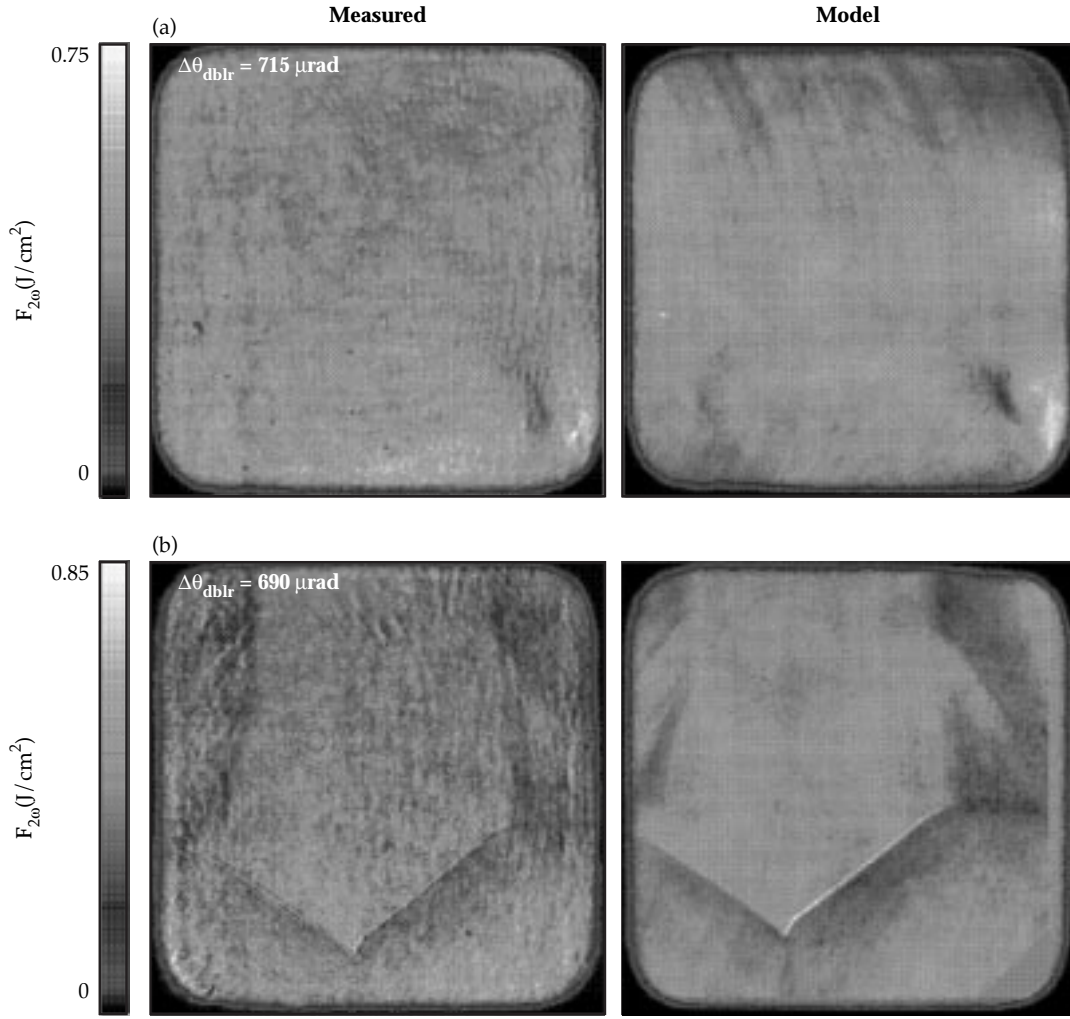


FIGURE 17. (a) Comparison of measured and modeled 2ω near-field distributions for conventional-growth doubler #345-1 at a drive irradiance of 3.9 GW/cm^2 . Measured and modeled conversion efficiencies were 6.7% and 6.5% respectively at an angular detuning of $715 \mu\text{rad}$ (internal angle). (b) Similar comparison for rapid-growth doubler #RG8B-2 at a drive irradiance of 4.2 GW/cm^2 . Measured and modeled conversion efficiencies were 6.6% and 7.0% respectively at an angular detuning of $690 \mu\text{rad}$. Sharp features in (b) are the boundaries between {101} (pyramidal) and {100} (prismatic) growth regions in the crystal; conventional growth material is all pyramidal. (70-00-0499-0795pb01)

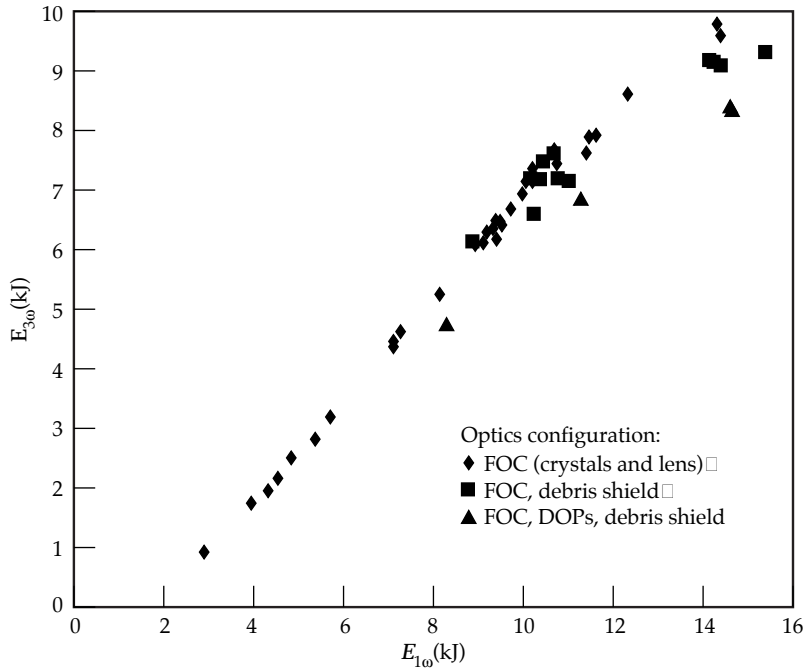


FIGURE 18. 3ω energy at the output of the final optics vs 1ω energy at the output of the laser amplifier, based on data obtained during the Beamlet high-energy test mule campaigns scaled to a NIF beam size of 1240 cm^2 . Pulse duration was 3 ns square. (70-00-0499-0796pb01)

Summary

Beamlet has contributed to NIF technology development in many areas and demonstrated important aspects of the NIF design. Near-field modulation experiments at high power have established the *B*-integral limits and spatial-filter pinhole sizes needed for controlling nonlinear ripple growth at high power and assuring safe operation without damage. High-contrast 20-ns pulses have been demonstrated at NIF-equivalent energy and power using prototypical pulse shaping technology. Pinhole designs have been developed and tested for spatial filtering. These experiments resulted in a $\pm 150\text{-}\mu\text{rad}$ SS cone baseline pinhole for the NIF, operating with neither closure nor back reflection. Detailed wavefront and far-field irradiance measurements demonstrated (1) that the Beamlet 3ω pulse meets spot-size criteria for NIF high-brightness missions, and (2) have provided a baseline for validating NIF propagation codes and establishing NIF optics specifications. In addition, efficient frequency conversion to the third harmonic was demonstrated with conventional and rapid-growth KDP/KD*P crystals in a prototypical NIF final optics configuration.

Acknowledgments

The authors gratefully acknowledge the many contributions from the large team of technicians, scientists, engineers, and administrative staff who made this work possible.

Notes and References

1. B. M. Van Wonterghem et al., *Appl. Opt.* **36**, 4932 (1997).
2. S. C. Burkhart, W. C. Behrendt, and I. Smith, *ICF Quarterly Report* 5(1), 68, Lawrence Livermore National Laboratory, Livermore, CA, UCRL-LR-105821-95-1 (1994).
3. J. A. Caird et al., "Beamlet focal plane diagnostic," *Proc. Soc. Photo-Opt. Instrum. Eng.* **3047**, 239 (1996).
4. J. B. Trenholme, *Laser Program Annual Report*, Lawrence Livermore National Laboratory, Livermore, CA, UCRL-50021-75, 237 (1975).
5. V. I. Bespalov and V. I. Talanov, *JETP Lett.* **3**, 307 (1966).
6. R. L. Carman, R. Y. Chiao, and P. L. Kelley, *Phys. Rev. Lett.* **17**, 1281 (1966).
7. E. S. Bliss, D. R. Speck, J. F. Holzrichter, J. H. Erkkila, and A. J. Glass, *Appl. Phys. Lett.* **25**, 448 (1974).
8. S. C. Burkhart, R. Wilcox, D. Browning, and F. Penko, "Amplitude and phase modulation with waveguide optics," *Proc. Soc. Photo-Opt. Instrum. Eng.* **3047**, 610 (1996).
9. P. M. Celliers et al., *Appl. Opt.*, **37**, 2371 (1998).
10. J. E. Murray, D. Milam, C. D. Boley, and K. G. Estabrook, "Spatial filter issues," presented at Solid State Lasers for Application to Inertial Confinement Fusion, Monterey, CA (1998).
11. D. Milam et al., "Pinhole closure measurements," presented at Solid State Lasers for Application to Inertial Confinement Fusion, Monterey, CA (1998).
12. J. E. Murray et al., "Spatial filter issues," *Proc. Soc. Photo-Opt. Instrum. Eng.*, **3047**, 207 (1996).
13. J. Murray et al., *ICF Quarterly Report* 7(3), 99, Lawrence Livermore National Laboratory, Livermore, CA, UCRL-LR-105821-97-3 (1997).
14. A. C. Erlandson, M. D. Rotter, D. N. Frank, and R. W. McCracken, *ICF Quarterly Report* 5(1), 18, Lawrence Livermore National Laboratory, Livermore, CA, UCRL-LR-105821-95-1 (1994).
15. M. D. Rotter, R. W. McCracken, A. C. Erlandson, and D. Brown, "Thermal recovery measurements on multi-segment amplifiers," *Proc. Soc. Photo-Opt. Instrum. Eng.* **2633**, 70 (1995).

16. R. Hartley et al., "Wavefront correction for static and dynamic aberrations to within 1 second of the system shot in the NIF Beamlet demonstration facility," *Proc. Soc. Photo-Opt. Instrum. Eng.* **3047**, 294 (1996).
17. J. T. Salmon et al., "An adaptive optics system for solid state lasers used in inertial confinement fusion," *Proc. Soc. Photo-Opt. Instrum. Eng.* **2633**, 105 (1995).
18. C. La Fiandra, P. Mehta, G. Goldstein, R. A. Zacharias, and S. Winters, "NIF deformable mirror," presented at Solid State Lasers for Application to Inertial Confinement Fusion, Monterey, CA (1998).
19. P. J. Wegner et al., "Wavefront and divergence of the Beamlet prototype laser," presented at Solid State Lasers for Application to Inertial Confinement Fusion, Monterey, CA (1998).
20. B. M. Van Wonterghem et al., "A compact and versatile pulse generation and shaping subsystem for high energy laser systems," *Proc. Soc. Photo-Opt. Instrum. Eng.* **1870**, 64 (1993).
21. J. K. Lawson et al., "NIF optical specifications—the importance of the RMS gradient," presented at Solid State Lasers for Application to Inertial Confinement Fusion, Monterey, CA (1998).
22. J. K. Lawson, D. M. Aikens, R. E. English Jr., and C. R. Wolfe, "Power spectral density specifications for high-power laser systems," *Proc. Soc. Photo-Opt. Instrum. Eng.* **2775**, 345 (1996).
23. W. H. Williams et al., "Modeling characterization of the National Ignition Facility focal spot," presented at LASE '98, San Jose, CA (1998).
24. R. E. English Jr., J. Miller, C. Laumann, and L. Seppala, *ICF Quarterly Report* **7**(3), 112, Lawrence Livermore National Laboratory, Livermore, CA, UCRL-LR-105821-97-3 (1997).
25. V. Karpenko et al., *ICF Quarterly Report* **7**(3), 166, Lawrence Livermore National Laboratory, Livermore, CA, UCRL-LR-105821-97-3 (1997).
26. P. J. Wegner et al., "Frequency converter development for the National Ignition Facility," presented at Solid State Lasers for Application to Inertial Confinement Fusion, Monterey, CA (1998).
27. N. P. Zaitseva et al., *J. Cryst. Growth* **180**, 255 (1997).
28. M. Kozlowski et al., "Laser damage performance of fused silica optical components measured on the Beamlet laser at 351 nm," Symposium on Optical Materials for High Power Lasers, Boulder, CO (1998).
29. P. J. Wegner et al., "Third-harmonic performance of the Beamlet prototype laser," *Proc. Soc. Photo-Opt. Instrum. Eng.* **3047**, 370 (1996).

